Dynamic Pressure Mapping of Personalized Handwriting by a Flexible Sensor Matrix Based on the Mechanoluminescence Process

Xiandi Wang, Hanlu Zhang, Ruomeng Yu, Lin Dong, Dengfeng Peng, Aihua Zhang, Yan Zhang, Hong Liu, Caofeng Pan,* and Zhong Lin Wang**

One of the most common methods for identity verifications is an electronic signature,[1] which is used for communication, commercial purposes, financial transactions, and many more. Current technology only records the handwriting graphics generated by the signees, while other information such as the local pressure/force applied during the signing process and the speed at which the letter was written are missed. It is such information that carries abundant personal identities that cannot be easily replicated by others, and can be uniquely used for identity verification to effectively prevent possible forgeries and fraud. Therefore, newly designed signature collectors are necessary to record more-personalized information during signing, with a widespread potential applicability in human–machine interfaces and artificial intelligence, which urges the development of large-size, high-spatial-resolution, highly sensitive, and fast-response pressure sensor arrays. A few groups have demonstrated pressure sensor arrays using assembled nanowires (NWs), organic transistors, or microstructured rubber layers based on the change in capacitance or resistance,[2] which can map strain distribution in a matrix format at a resolution in the order of millimeter-scale. In our previous work, we have developed a large-array of 92 × 92 piezotronic transistors based on vertical ZnO NWs and an array of over 20 000 n-ZnO/p-GaN piezotronic light-emitting diodes (LEDs) as an active taxel-addressable pressure/force-sensor matrix for tactile imaging at a resolution of 2.7 μm.[3] However, this research can only serve as static pressure mapping, and cannot realize a dynamic mapping which is needed to get the large scale pressure distribution in a very short time of as little as tens of milliseconds.

X. Wang, H. Zhang, Prof. L. Dong,
Dr. D. Peng, Dr. A. Zhang, Prof. Y. Zhang,
Prof. H. Liu, Prof. C. Pan, Prof. Z. L. Wang
Beijing Institute of Nanoenergy and Nanosystems
Chinese Academy of Sciences
Beijing 100083, PR China
E-mail: donglin@binn.cas.cn;
cfpan@binn.cas.cn; zhong.wang@mse.gatech.edu
H. Zhang, Prof. L. Dong
School of Materials Science & Engineering
Zhengzhou University
Zhengzhou 450001, PR China
R. Yu, Prof. Z. L. Wang
School of Materials Science and Engineering
Georgia Institute of Technology
Atlanta, GA 30332–0245, USA

DOI: 10.1002/adma.201405826

Here we introduce a wafer-scale, flexible pressure sensor matrix (PSM) for securer signature collections by recording both the handwritten graphics and the signing habits (e.g., pressure/force applied at each pixel during signing; signing speed) of the signee. The implementations of these features are based on the mechanoluminescence (ML) of ZnS:Mn particles (ZMPs) for instantaneous mapping of pressure of both a single-point and a 2D planar distributions ranging from 0.6–50 MPa through a conversion process between mechanical stress and visible light emissions.[4] Furthermore, piezophotonic effect,[5] known as a two-way coupling effect between piezoelectricity and photoexcitation properties, is proposed to initiate the ML process during this conversion. Under pressures, piezoelectric polarization charges are induced within piezoelectric ZnS due to its noncentral symmetry.[3b,6] The potential produced by the piezo-charges effectively tilts the band structure and thus facilitates the detrapping of electrons into the conduction band of ZMPs.[7] Recombination between detrapped electrons and holes hence occurs; the energy is released to excite the dopant Mn^{2+} ions instead of emitting a photon. When the excited Mn^{2+} ion falls back to its ground state, a photon is emitted as yellow color visible light. Therefore, strain-induced piezoelectric potential plays an essential role in bending the band structure within ZMPs, and thus tune/control the photoexcitation process. Following this working mechanism, visible light emissions are observed immediately after applying a local force/pressure on the device, leading to a high-definition two-dimensional (2D) pressure mapping of the dynamic signing process with time-response of 10 ms and spatial-resolution of less than 100 μm (254 dpi). Furthermore, this PSM device is self-powered and requires no external electric power for operations. The PSM devices may find potential applications in real-time pressure mapping systems, smart sensor networks, high-level security systems, and human–machine interfaces.

The PSM devices are fabricated by employing wurtzite-structure ZnS:Mn particles as mechanoluminescent materials in the middle, sandwiched by two polymeric layers at top and bottom for packaging as shown schematically in **Figure 1**a. Poly(ethylene terephthalate) (PET) film serves as the protective layer due to its outstanding toughness; the thermoplastic ethylene–vinyl acetate copolymer (EVA) is applied to bond ZMPs tightly with PET films after heat sealing (see Experimental Section). These transparent polymeric layers are favorable to the transmission of yellow light emitted by ZMPs under pressure. Determined by a systematical study of the materials synthesis process (details can be found in Section A, Supporting

© 2015 WILEY-VCH Verlag GmbH & Co. KGaA, Weinheim

ADVANCED MATERIALS
www.advmat.de

www.MaterialsViews.com

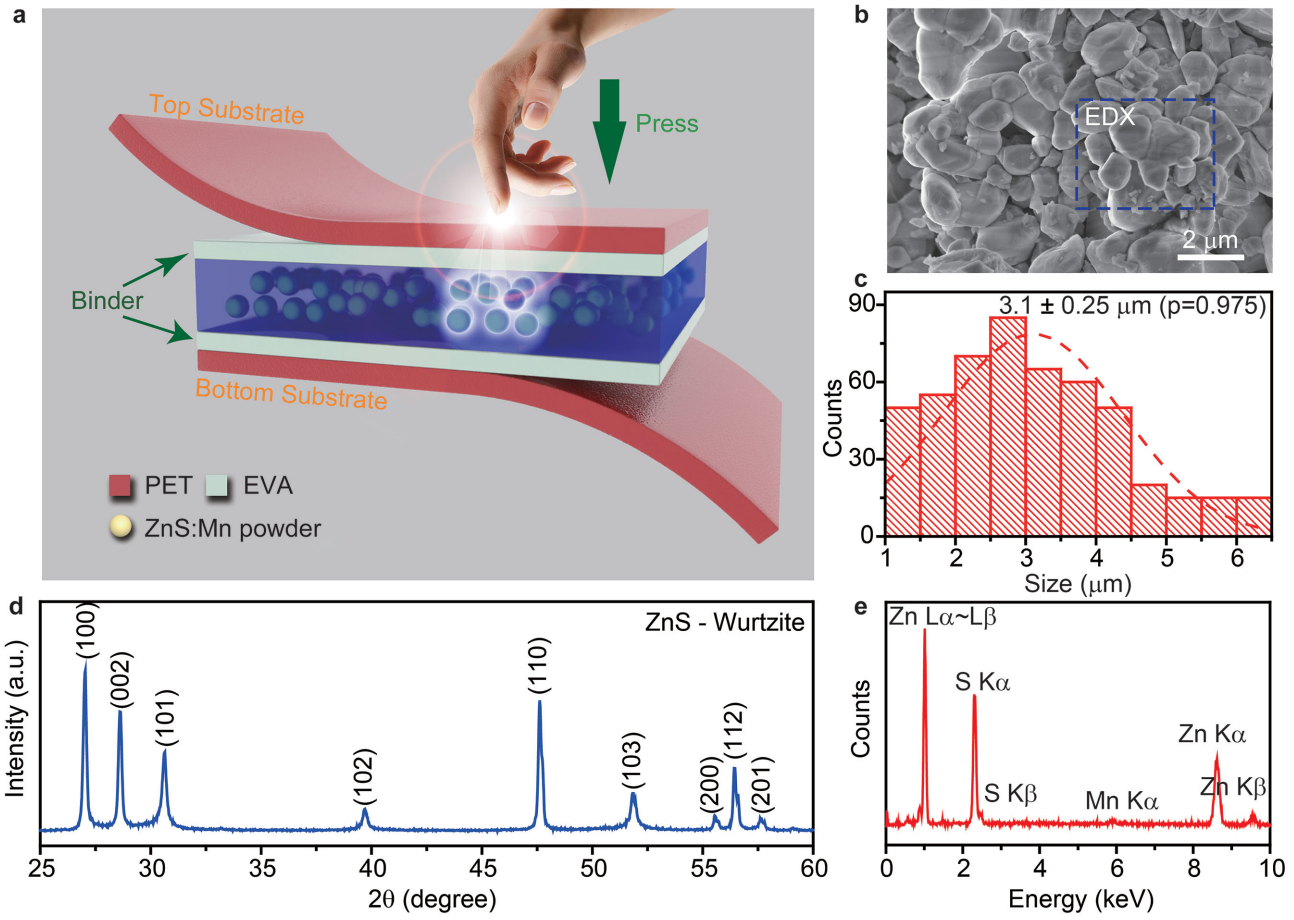

Figure 1. Schematic structure of PSM devices and characterization of ZnS:Mn particles. a) Schematic configuration of PSM devices. b) SEM image of the grounded ZnS:Mn particles doped with 1 at% Mn^{2+} ions by a vacuum solid state reaction at 1050 °C for 3 h. c) Statistical results of ZMP sizes with a mean value of 3.1 ± 0.25 mm (97.5% confidence interval). d) X-ray diffraction (XRD) pattern of ZnS powder samples, showing a typical wurtzite structure (JCPDS no. 36–1450). e) Energy dispersive X-ray spectrum (EDX) of the sample, confirming the existence of the element Mn in the sample.

Information), ZnS:Mn particles with optimized ML properties are doped with 1 at% Mn^{2+} ions via a vacuum solid-state reaction sintered at 1050 °C for 3 h. The morphology of the as-synthesized ZMPs is characterized by scanning electron microscopy (SEM) as presented in Figure 1b. By grinding and screening, the mean size of obtained ZMPs is calculated and summarized in Figure 1c as 3.1 ± 0.25 μm (97.5% confidence interval). X-ray powder diffraction (XRD) (Figure 1d) confirms the wurtzite structure (JCPDS no. 36–1450) of ZnS. A small peak of Mn K_α is observed in the energy dispersive spectrum (EDX) of the product shown in Figure 1e. No other diffraction peak of manganese compounds or impurity is found from the XRD pattern. Therefore, we confirm the existence of element Mn in the acquired ZMPs.

The ML features of these PSM devices are carefully investigated by applying different pressures/strains on them. A typical ML spectrum derived from a device (0.5 g ZMPs, 0.1 mm-thick PET) under a series of loaded forces are presented in **Figure 2**a, indicating a fixed peak value near 585 nm (yellow light) within the emission range of 525–685 nm. The peak intensity at 585 nm and the integral intensity over 525–685 nm are summarized in Figure 2b for each corresponding loaded force condition (ranging from 0.8 to 10 N), showing that emission intensity increases with applied forces in both cases. Besides, by converting forces into pressures, the integral intensity versus external pressures is plotted in Figure 2c, and the slope of the curve is defined as the sensitivity of the PSM device, and exhibits an obvious linearly increasing trend in the range of 10–50 MPa. After a standard calibration, the location and the magnitude of pressure applied to the device can be precisely determined by parallel reading out of the position and intensity of light emissions produced through the ML process of our PSM devices. Moreover, the lowest threshold pressure of 600 kPa is derived for detectable ML intensity (Figure S3, Section B, Supporting Information), implying numerous prospective applications of these PSM pressure mapping devices.

Although various mechanisms have been proposed for the ML process,[7c,8] two opinions are the most accepted: i) the emission peak near 585 nm is resulted from the $^4T_1$ (^4G)–$^6A_1$ (^6S) transitions of Mn^{2+} ions;[9] ii) the piezoelectric potential plays a crucial role in the ML process of ZMPs.[7a,10] Based on this understanding, we propose the piezophotonic effect to explain the physical mechanism behind the observed ML behavior of ZMP-based PSM devices.[5] As a two-way coupling effect between

© 2015 WILEY-VCH Verlag GmbH & Co. KGaA, Weinheim

DOI: 10.1002/adma.201405826

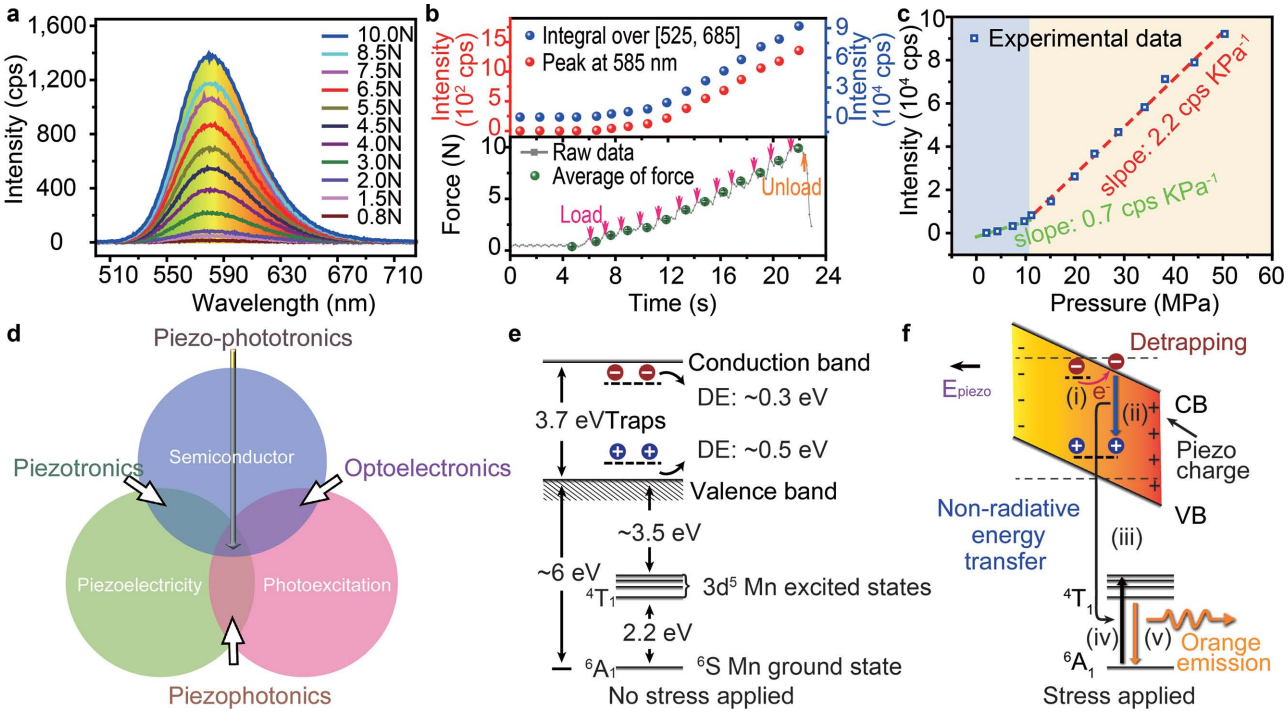

Figure 2. Mechanoluminescence features and proposed working mechanism. a) ML spectra under different applied forces, derived from a PSM device with 0.5 g ZMPs and 0.1 mm-thick PET films. b) Peak intensity at 585 nm (red dots) and integral intensity over 525–685 nm (blue dots) versus averaged forces as indicated in the bottom panel (green dots). c) Integral intensity over 525–685 nm under different pressures. d) Schematic diagram showing the field of piezotronics, optoelectronics, piezophototronics, and piezophotonics. e) Schematic illustration of band diagram of Mn-doped ZnS. f) The piezophotonic effect initiated the ML process. Strain-induced piezo-potential facilitate the detrapping of electrons (i); non-radioactive recombination between detrapped electrons and holes transfer energy to Mn^{2+} ions (ii)–(iv); excited Mn^{2+} ions fall back to the ground state with visible light emissions (v).

piezoelectricity and photoexcitation properties (Figure 2d), the piezophotonic effect is considered to initiate the ML process during the conversion from mechanical stress to visible light emission. Upon straining, piezoelectric polarization charges are induced within wurtzite-structure piezoelectric ZnS due to its noncentral symmetry. At the dopant site,[11] the first principle calculation (Figure S4, Section C, Supporting Information) shows that an electron defect state and a hole defect state are created by Mn doping, with the upper state trapping electrons and the lower state trapping holes. Once a mechanical stress is applied, the conduction and valence bands of ZnS are tilted due to the potential produced by the piezo-charges. As a result, the trapped electrons in the upper electron defect state become much easier to be detrapped and released into the conduction band of ZMPs (Figure 2f).[7] Then a non-radioactive recombination occurs between detrapped electrons and holes by transferring energy (≈2.8 eV) to the Mn^{2+} ion and exciting its outer shell electrons from $^6A_1$ (^6S) to $^4T_1$ (^4G), (required energy 2.2–2.5 eV) (Figure 2e,f). When the excited electrons of Mn^{2+} ions fall back to the $^6A_1$ (^6S), photons are emitted as yellow color visible light.[4c] Therefore, the strain-induced piezoelectric potential plays an essential role in tilting the band structure within ZMPs, and thus tunes/controls the photoexcitation process. This is the piezophotonic effect. The significance of piezoelectric potential proposed in this working mechanism is further verified by comparing the ML intensities between the devices composed of wurtzite (with higher piezoelectric coefficient) and zinc-blende (with lower piezoelectric coefficient) ZMPs under the similar pressure (Figure S5, Section D, Supporting Information). It is obvious that the device fabricated with wurtzite ZMPs shows 20 times stronger ML intensities, compared with the device composed of zinc blend ZMPs. Following this working mechanism, visible light emissions are observed immediately after applying forces on the PSM device; detecting the emitted light gives a real-time, high-spatial and time resolution 2D pressure dynamic mapping of the handwriting across the device.[2a-d]

Aiming at practical applications, the stability and repeatability of PSM devices are carefully investigated and presented in **Figure 3**a by applying a periodic 15 MPa pressure on the device for more than 10 000 cycles. Generally, these PSM devices display a stable ML intensity throughout the whole test, except for the initial damping (before 1000 cycles) that may be interpreted by the condensation and stabilization of ZMPs during the deformations at the beginning. Moreover, the flexibility and mechanical robustness of PSM devices are studied by a cyclical bending test, in which the PSM device is attached to a linear motor moving back and forth, as shown in Figure 3b,c. Neither apparent decrease in ML intensity nor obvious physical damages of the device is observed after each thousand bending cycles (Figure 3b). These results clearly indicate the robustness of our PSM devices in both mechanical and ML properties after a long period of operations, making them reliable for practical applications.

© 2015 WILEY-VCH Verlag GmbH & Co. KGaA, Weinheim

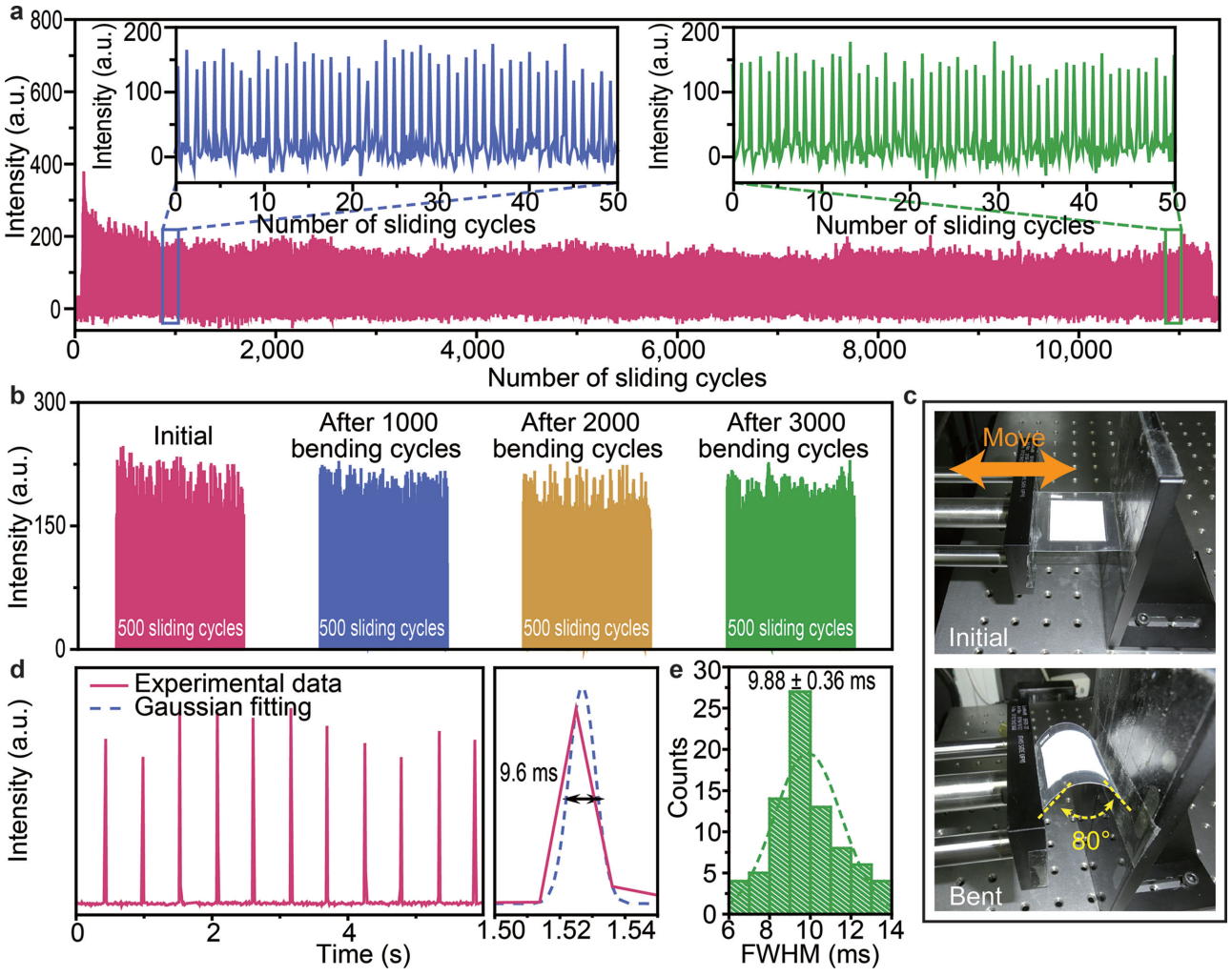

Figure 3. PSM devices characterization. a) Stability and repeatability test of PSM devices (0.5 g ZMPs, 0.1 mm-thick PET films) bent by more than 10 000 cycles. b) Robustness and c) flexibility test of PSM devices (0.5 g ZMPs, 0.1 mm-thick PET films) for more than 3000 cycles. d) Response time of PSM devices under dynamic pressures mapping test with Gaussian fittings. e) Statistic result of response time with 9.88 ± 0.36 ms (97.5% confidence interval).

The accomplishment of real-time pressure mapping highly depends on the fast response time of our PSM devices. Considering the full-width at half-maximum (FWHM) of ML intensities, the response time is calculated and summarized in Figure 3d, followed by Gaussian fittings. The statistic result of response time at FWHM from 80 measurements indicates a mean value of 9.88 ± 0.36 ms (97.5% confidence interval), as shown in Figure 3e. Given the time resolution of our spectrometer being 8 ms, the real response time of our PSM devices can be much shorter. By parallel reading out of the optical signals emitted during the pressure sensing process, real-time pressure mapping is achieved based on this fast response time, which provides a huge advantage against those electrical-signal processing devices.

Under both a single-point dynamic pressure recording and a 2D planar pressures mapping modes, the ZMP-based PSM devices immediately respond via the ML process to convert mechanical stress into light emission. By parallel recording and processing the optical signals, detailed 2D pressure distributions are visualized in real-time through an image acquisition and processing system as shown in **Figure 4**a. A charge-coupled device (CCD) image sensor is connected to a personal computer to capture light emissions from PSM devices under pressures, as the image acquisition unit; a self-developed computer software is utilized to process the acquired images for pressure mapping, as the signal processing unit. 2D planar pressure visualization is demonstrated in Figure 4b by pressing a "rose-shape" stamp on the PSM device. Dynamic pressure visualization is presented in Figure 4c by capturing a handwritten letter "e" in real-time. The corresponding 2D distributions of relative ML intensity are derived by extracting the gray scale of the real-time captured image, as shown in Figure 4d. The line profile of the region marked by the green rectangle (Figure 4d), presented in Figure 4e, clearly reveals the difference of relative intensity between points A and B, suggesting the capability of acquiring detailed pressure information by PSM devices from handwritten signatures to analyze the signing habits of signees for securer signature collection applications. Moreover, the

© 2015 WILEY-VCH Verlag GmbH & Co. KGaA, Weinheim
Adv. Mater. **2015**,
DOI: 10.1002/adma.201405826

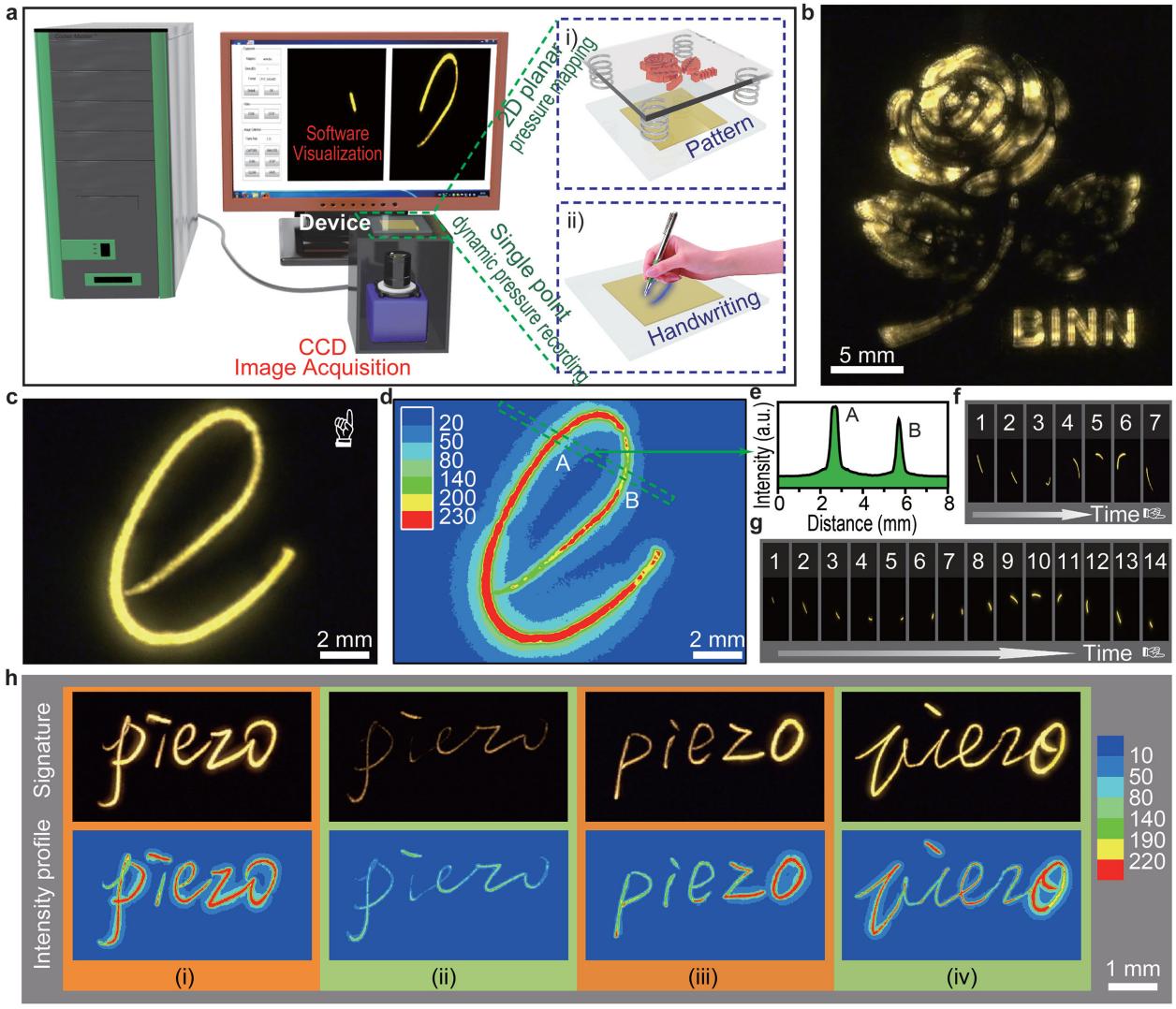

Figure 4. Visualization of dynamic pressure distributions. a) Schematic illustration of the image acquisition and processing system: i) 2D planar pressure mapping and ii) single-point dynamic pressure recording measurements. b) Visualization of 2D planar pressure distributions generated by a stamp. c) Visualization of dynamic pressure distributions generated from a handwritten "e". d) The corresponding 2D distribution of relative ML intensity derived by extracting gray scale from (c). e) The line profile of relative ML intensity from the marked area in (d). f,g) Consecutive frames extracted from the dynamically capture video of the signing process based on a 80 ms time interval to reveal the signing speed: f) fast signing speed; g) slow signing speed. h) Demonstrations of recording the signing habits of four signees by PSM devices. Pressure evenly distributed to every point during the signing process, with strong force (i); pressure evenly distributed to every point during the signing process, with weak force (ii); more pressures applied at the end of the signing process (iii); more pressure applied at the end and some turning points of the signing process (iv).

signing speed can also be monitored dynamically by counting the number of frames extracted from the captured video for the signing process based on a certain time interval. Controlled by a computer program, frames at a time interval of 80 ms are extracted from the dynamically captured signing video and superposed to display as several consecutive images, as shown in Figure 4f,g. Fewer images are derived for a signee with faster signing speed (Figure 4f), and more images are derived for a signee with slower signing speed (Figure 4g). In this manner, our PSM devices can precisely monitor the signing speed of each signee, which is another critical parameter to analyze the signing habits for high-level security purposes.

A demonstration of our securer signature collection system using these ZMP-based PSM devices to record both handwritten signatures and the signing habits of a few signees is presented in Figure 4h. Based on the handwritten signatures "piezo" and the corresponding relative ML intensity distribution maps collected from four signees (Figure 4h), the morphological differences among the four signatures are obvious. Our PSM devices are capable of providing more personalized writing behavior, such as pressure applied on each pixel when signing and signing speed. As shown in Figure 4h, the first and second signee both intended to sign steadily with pressures evenly distributed through the whole signing process, while the

© 2015 WILEY-VCH Verlag GmbH & Co. KGaA, Weinheim

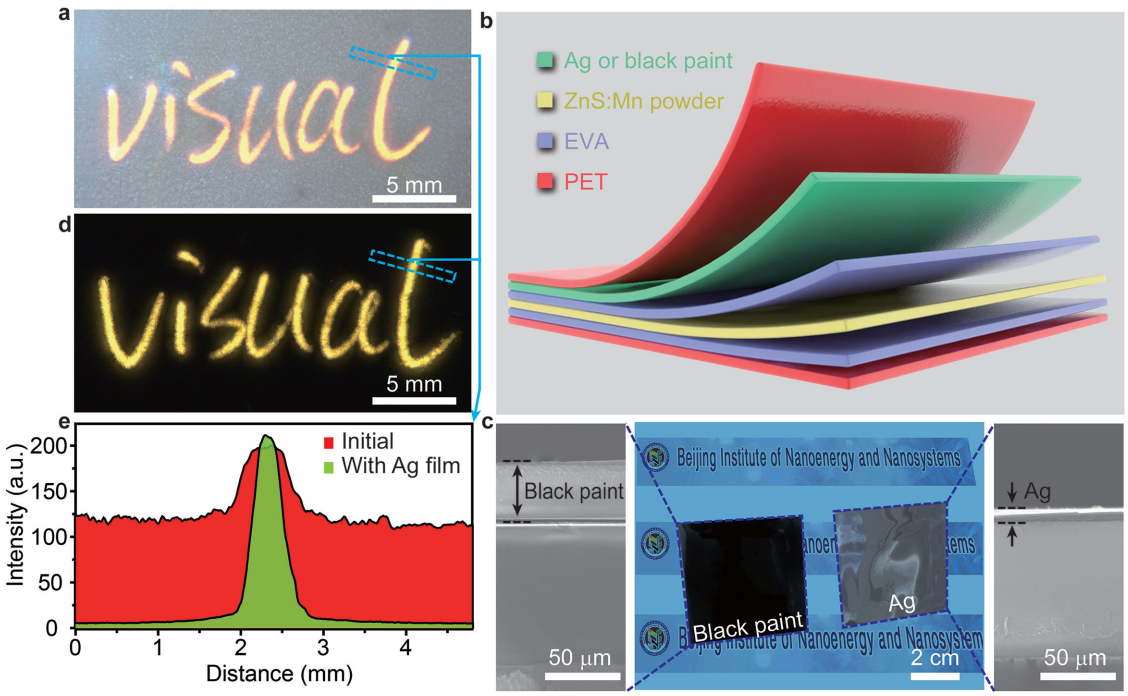

Figure 5. Improvements on SNR. a) Performances of PSM devices without a light blocking layer for dynamic pressure mappings under 100 mW cm^{-2} light illumination. b) Schematic configuration of modified PSM devices with a light blocking layer. c) Morphology of the modified device. A cross-sectional SEM image of the PET film with a 50 mm-thick black paint blocking layer (left panel) and 3 mm-thick Ag film blocking layer (right panel). d) Performances of PSM devices with a light blocking layer for dynamic pressure mappings under 100 mW cm^{-2} light illumination. e) ML intensity line profile to illustrate the SNR of PSM devices without (red) and with (green) a light blocking layer.

first signee (Figure 4h(i)) obviously signed with a stronger force than the second signee (Figure 4h(ii)) did. The third signee (Figure 4h(iii)) applied more pressures at the end of the signing process, and the forth signee (Figure 4h(iv)) preferred signing with more pressures both at the end and some turning points of the signing process. Therefore, both the handwritten signatures and the signing habits of signees are recorded by these PSM devices.

Although the PSM device can operate under bright illuminations, the signal-to-noise ratio (SNR) is relatively low as shown in **Figure 5**a,e (red). A light blocking layer is therefore assembled on the inner side of the top PET layer (Figure 5b) to improve the SNR by either reflecting (silver film, Figure 5c) or absorbing (black paint, Figure 5c) the incident environmental light. Under the same signing and illumination conditions adopted in Figure 5a, improved PSM device with a light blocking layer displays a much better SNR as shown in Figure 5d,e (green).

The spatial resolution of PSM devices depends on the micropatterning technology employed during the fabrication process. In this work, we demonstrate a pressure mapping resolution of 100 μm through a UV photolithography technique as illustrated in **Figure 6**a. The large-scale mechanoluminescent ZMPs:photoresist arrays are fabricated on PET substrate through standard photolithography processes by mixing ZMPs with a photoresist (Experimental Section). The entire device is packaged by another layer of EVA and PET to protect it from contamination and damage (Figure 6a). The digital image of a transparent PSM device is shown in Figure 6b. The detailed dimensions of this device are characterized by SEM in top (Figure 6c) and side (Figure 6d,e) views, showing a 50 μm × 50 μm ML pixel size with 100 μm center-to-center distance. The cross-section SEM images (Figure 6d,e) clearly indicate a layered structure and a pixel height of 13 μm. Dynamic pressure mappings are demonstrated by signing "nano" on top of this device as shown in Figure 6f,g. An enlarged view of the marked area (red rectangular in Figure 6g) is displayed in Figure 6h, clearly showing distinguishable light emissions from pixels under pressures. The ML intensity distributions of 20 pixels collected from both horizontal and vertical directions (indicated by the purple and red arrows in Figure 6h) confirm the elimination of crosstalk between adjacent pixels. Light emission is merely observed from pixels under pressure, while no optical signals are collected from others. These outstanding features greatly benefit the pressure mapping applications in accuracy. Therefore, PSM devices provide a new approach for real-time, high-resolution pressure mapping in both single-point dynamic pressure recording and 2D planar pressure mapping.

Our ZMP-based PSM devices provide a securer approach for intelligent electronic signature collections compared with conventional technologies. Not only the handwritten signatures, but also the unique signing behaviors of the signees are simultaneously recorded by these PSM devices. Both the dynamic pressure distributions and the signing speed at each pixel during the signing process are fully recorded by PSM devices to support the analysis of different signees' signing habits. These functions provide different paths for electronic signature collection technologies to fulfill high-level security demands.

© 2015 WILEY-VCH Verlag GmbH & Co. KGaA, Weinheim
Adv. Mater. **2015**,
DOI: 10.1002/adma.201405826

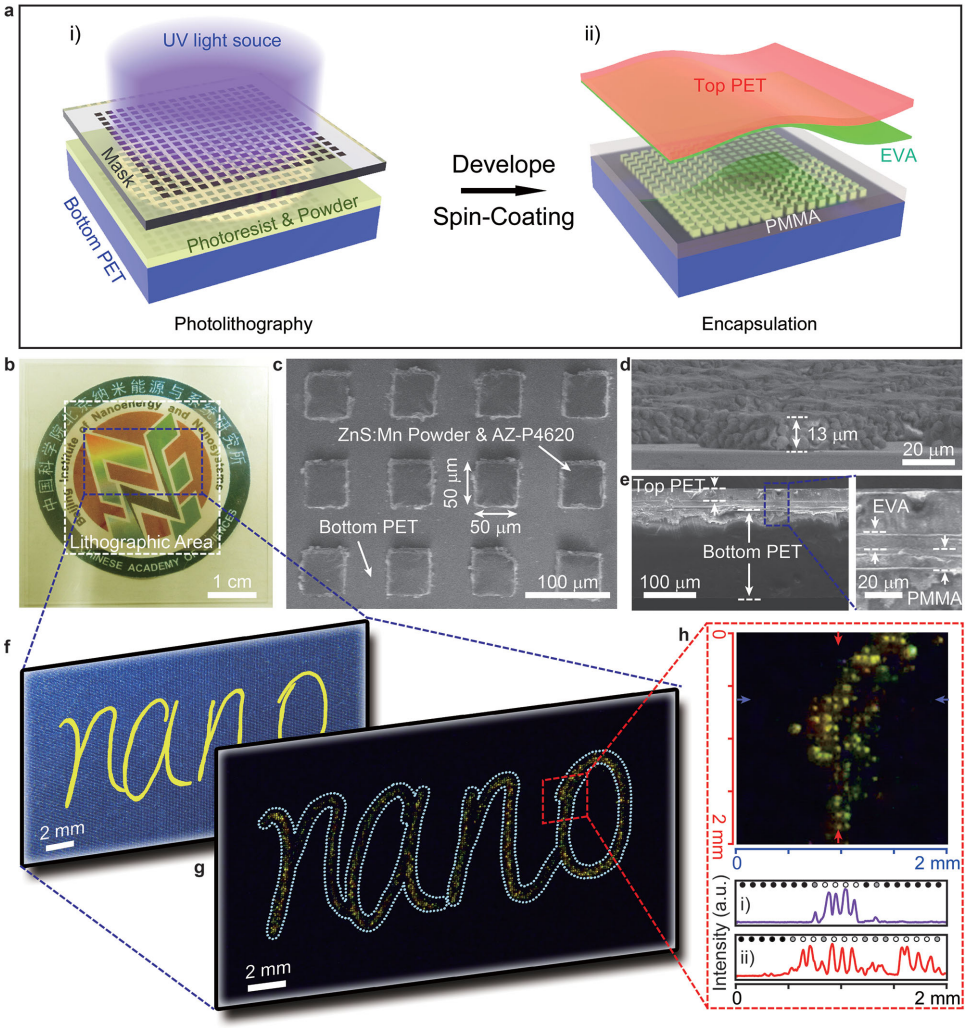

Figure 6. Spatial resolution. a) Schematic illustration of the UV photolithography fabrication process of PSM devices. b) A digital image of a transparent PSM device. c–e) SEM images of ZMPs:photoresist array-structured PSM devices in top (c) and side (d,e) views. Pixel size is 50 mm × 50 mm in area, 13 mm in height, 100 mm in center-to-center distance. f,g) Visualization of dynamic pressure distributions generated from a handwriting "nano" by array-structured PSM devices. h) Enlarged view of marked area in (g). Bottom panel: line profile of ML intensity of pixels in horizontal (indicated by the purple arrows) and vertical (indicated by the red arrows) directions, no cross-talk between adjacent pixels are observed, showing a good resolution and distinguishability.

In summary, we introduce a ZnS:Mn ML particles based pressure sensor matrix device for both single-point dynamic pressure recording and 2D planar pressure mapping in the range of 0.6–50 MPa using self-generated light emission without an external power source. The mechanism is suggested due to the piezophotonic effect as a result of piezopotential induced light emission from the dopant element. A fast response time less than 10 ms and a high spatial resolution of 100 μm (254 dpi) are achieved from these PSM devices to guarantee outstanding performances both in stability and repeatability after thousands of cycles of testing. These PSM devices are demonstrated for securer electronic signature collections by recording both the handwritten signatures and the signing behavior/habits of the signees. Compared with the existing technologies, our devices collect more, unique and reliable personalized information during the signing process, providing a new approach to fulfill high-level security. Our PSM devices may find prospective applications in real-time pressure mappings, smart sensor networks, high-level security systems and human–machine interfaces.

Experimental Section

Synthesis and Characterization of ZnS:Mn Particles: The ZnS:Mn particles were prepared via a vacuum solid state reaction. Briefly, $MnCO_3$ (99.95%, Aladdin) and ZnS (99.99%, Aladdin) powders were mixed in various ratios by wet grinding, with ethanol as dispersion medium. Next, the mixed raw powders were loaded into an alumina boat compactly and sintered at a series of temperatures and reaction time in vacuum, details are found in Section A, Supporting Information. After determining the optimized parameters for ZMPs synthesizing, the mechanoluminescent ZnS:Mn particles used for PSM device fabrications were collected by further grinding and screening. The crystallization of the powders was characterized by X-ray diffraction (XRD) θ–2θ scan with Cu-K_α radiation using Rigaku TTR diffractometer. The morphology and the elemental

© 2015 WILEY-VCH Verlag GmbH & Co. KGaA, Weinheim

components of the samples were investigated by field-emission scanning electron microscopy (FESEM) (Hitachi SU8020) equipped with energy dispersive X-Ray spectroscopy (EDX) (IXRF SDD2830–300D).

Fabrication of PSM Devices: The PSM devices demonstrated in this work were mainly fabricated through two different types of processes, "emulsion deposition" and "UV photolithography." As for the "emulsion deposition" method, the synthesized ZMPs were ultrasonically dispersed in ethanol, followed by a rapid transfer onto a 5 cm × 5 cm sized EVA-covered PET thin film, whose edges were enclosed by a rectangular frame mold. After the volatilization of ethanol, a flat lamina of ZnS:Mn particles with great uniformity was deposited on the film. Subsequently, the film was covered by another piece of EVA-covered PET film face-to-face and sent into a thermal laminator for packaging. As for the "UV photolithography" method, carefully grounded ZnS:Mn microparticles were homogeneously mixed with positive photoresist (AZ P4620) at the weight ratio of 1:3. Next, the mixed compound was spin-coated onto a 5 cm × 5 cm sized clean PET thin film, followed by UV photolithography to construct precisely aligned ZMPs:photoresist compound arrays with center-to-center pitch of 100 μm. Then, a layer of poly(methyl methacrylate) (PMMA) was spin-coated onto the compound arrays to prevent structural damages. Finally, the device with arrayed ML structures was packaged with another piece of EVA-covered PET film in a similar way as described above.

ML Measurements: A home-made measuring system was built to collect ML spectrum and value of applied force on PSM devices. In this system, a pen was fixed on a linear motor to apply periodic pressures on the device by moving the pen tip back and forth repeatedly. Light emissions were collected from the contact point by a spectrometer (Ocean Optics QE65pro) in the range of 200–900 nm. The vertical contact force was measured by a pressure sensor (ATI Nano17).

Supporting Information

Supporting Information is available from the Wiley Online Library or from the author.

Acknowledgements

X.W., H.Z., and R.Y. contributed equally to this work. The authors acknowledge the support from the "Thousands Talents" program for pioneer researcher and his innovation team, China; President Funding of the Chinese Academy of Sciences, National Natural Science Foundation of China (Grant Nos. 51272238, 21321062, 51432005, and 61405040), the Innovation Talent Project of Henan Province (Grant No. 13HASTIT020), Talent Project of Zhengzhou University (ZDGD13001), and Surface Engineering Key Lab of LIPCAST.

Received: December 20, 2014
Revised: February 3, 2015
Published online:

[1] a) J. J. Boland, *Nat. Mater.* **2010**, *9*, 790; b) J. Y. Hwang, S. Lee, B. H. Chung, H. S. Cho, D. Nyang, *Information Sci.* **2013**, *222*, 761; c) S. Viriri, J. R. Tapamo, *Sensors* **2012**, *12*, 4324.

[2] a) D. J. Lipomi, M. Vosgueritchian, B. C. K. Tee, S. L. Hellstrom, J. A. Lee, C. H. Fox, Z. N. Bao, *Nat. Nanotechnol.* **2011**, *6*, 788; b) K. Takei, T. Takahashi, J. C. Ho, H. Ko, A. G. Gillies, P. W. Leu, R. S. Fearing, A. Javey, *Nat. Mater.* **2010**, *9*, 821; c) S. C. B. Mannsfeld, B. C. K. Tee, R. M. Stoltenberg, C. V. H. H. Chen, S. Barman, B. V. O. Muir, A. N. Sokolov, C. Reese, Z. N. Bao, *Nat. Mater.* **2010**, *9*, 859; d) T. Someya, T. Sekitani, S. Iba, Y. Kato, H. Kawaguchi, T. Sakurai, *Proc. Natl. Acad. Sci. USA* **2004**, *101*, 9966; e) M. Segev-Bar, H. Haick, *ACS Nano* **2013**, *7*, 8366; f) M. Segev-Bar, A. Landman, M. Nir-Shapira, G. Shuster, H. Haick, *ACS Appl. Mater. Interfaces* **2013**, *5*, 5531; g) Q. Shao, Z. Q. Niu, M. Hirtz, L. Jiang, Y. J. Liu, Z. H. Wang, X. D. Chen, *Small* **2014**, *10*, 1466; h) B. W. Zhu, Z. Q. Niu, H. Wang, W. R. Leow, H. Wang, Y. G. Li, L. Y. Zheng, J. Wei, F. W. Huo, X. D. Chen, *Small* **2014**, *10*, 3625.

[3] a) W. Z. Wu, X. N. Wen, Z. L. Wang, *Science* **2013**, *340*, 952; b) C. F. Pan, L. Dong, G. Zhu, S. M. Niu, R. M. Yu, Q. Yang, Y. Liu, Z. L. Wang, *Nat. Photonics* **2013**, *7*, 752.

[4] a) A. J. Walton, *Adv. Phys.* **1977**, *26*, 887; b) B. P. Chandra, *Luminescence of Solids*, Plenum Press, New York **1998**, p. 361; c) C. N. Xu, T. Watanabe, M. Akiyama, X. G. Zheng, *Appl. Phys. Lett.* **1999**, *74*, 1236; d) N. C. Eddingsaas, K. S. Suslick, *Nature* **2006**, *444*, 163; e) C. G. Camara, J. V. Escobar, J. R. Hird, S. J. Putterman, *Nature* **2008**, *455*, 1089; f) S. M. Jeong, S. Song, S. K. Lee, N. Y. Ha, *Adv. Mater.* **2013**, *25*, 6194; g) S. M. Jeong, S. Song, K. I. Joo, J. Kim, S. H. Hwang, J. Jeong, H. Kim, *Energy Environ. Sci.* **2014**, *7*, 3338.

[5] a) Z. L. Wang, *Adv. Funct. Mater.* **2008**, *18*, 3553; b) Z. L. Wang, *Nano Today* **2010**, *5*, 540.

[6] a) R. M. Yu, L. Dong, C. F. Pan, S. M. Niu, H. F. Liu, W. Liu, S. Chua, D. Z. Chi, Z. L. Wang, *Adv. Mater.* **2012**, *24*, 3532; b) C. K. Jeong, K. I. Park, J. Ryu, G. T. Hwang, K. J. Lee, *Adv. Funct. Mater.* **2014**, *24*, 2620.

[7] a) B. P. Chandra, R. N. Baghel, V. K. Chandra, *Chalcogenide Lett.* **2010**, *7*, 1; b) D. O. Olawale, T. Dickens, W. G. Sullivan, O. I. Okoli, J. O. Sobanjo, B. Wang, *J. Lumin.* **2011**, *131*, 1407; c) B. P. Chandra, C. N. Xu, H. Yamada, X. G. Zheng, *J. Lumin.* **2010**, *130*, 442.

[8] a) G. Alzetta, N. Minnaja, S. Santucci, *Nuovo Cimento* **1962**, *23*, 910; b) I. Chudacek, *Czech. J. Phys.* **1967**, *17*, 34; c) J. I. Zink, *Acc. Chem. Res.* **1978**, *11*, 289.

[9] R. N. Bhargava, D. Gallagher, X. Hong, A. Nurmikko, *Phys. Rev. Lett.* **1994**, *72*, 416.

[10] Y. Zhang, G. Y. Gao, H. L. W. Chan, J. Y. Dai, Y. Wang, J. H. Hao, *Adv. Mater.* **2012**, *24*, 1729.

[11] a) R. Weidemann, H. E. Gumlich, M. Kupsch, H. U. Middelmann, *Phys. Rev. B* **1992**, *45*, 1172; b) R. Parrot, D. Boulanger, M. N. Diarra, U. W. Pohl, B. Litzenburger, H. E. Gumlich, *Phys. Rev. B* **1996**, *54*, 1662; c) H. E. Gumlich, R. L. Pfrogner, J. C. Shaffer, F. E. Williams, *J. Chem. Phys.* **1966**, *44*, 3929.

© 2015 WILEY-VCH Verlag GmbH & Co. KGaA, Weinheim